

Room-Temperature Magnetism in 2D MnGa₄-H Induced by Hydrogen Insertion

Nan Wei, Liangcheng He, Changwei Wu, Dabiao Lu, Ruohan Li, Haiwen Shi, Haihui Lan, Yao Wen, Jun He, Youwen Long,* Xiao Wang,* Mengqi Zeng,* and Lei Fu*

2D room-temperature magnetic materials are of great importance in future spintronic devices while only very few are reported. Herein, a plasma-enhanced chemical vapor deposition approach is exploited to construct the 2D room-temperature magnetic MnGa₄-H single crystal with a thickness down to 2.2 nm. The employment of H₂ plasma makes hydrogen atoms can be easily inserted into the MnGa₄ lattice to modulate the atomic distance and charge state, thereby ferrimagnetism can be achieved without destroying the structural configuration. The as-obtained 2D MnGa₄-H crystal is high-quality, air-stable, and thermo-stable, demonstrating robust and stable room-temperature magnetism with a high Curie temperature above 620 K. This work enriches the 2D room-temperature magnetic family and opens up the possibility for the development of spintronic devices based on 2D magnetic alloys.

construction of tedious devices, which seriously impedes the realization of reliable and convenient 2D magnetic phase/state modulation. To conquer such challenges, innovative effective methods necessitate further exploration toward realizing 2D magnetism, especially at room temperature.

The hydrogen atom is the smallest and lightest atom, and it can be easily inserted into the interstitial sites of the host lattice. Meanwhile, 2D material is considerably sensitive to lattice variations. It is expected that effective magnetic modulation can be achieved by inserting hydrogen atoms into the 2D material lattice. 2D Metals are ideal hosts due to the large lattice distance

and flexible structure that can ensure hydrogen atoms easily enter their host lattice without embrittlement.^[18] Moreover, 2D magnetic metals can be used to fabricate spintronic devices while the relevant research is still in its infancy. The strong metallic bonding of non-layered metals hinders the layer-by-layer mechanical exfoliation or 2D anisotropic growth, and even worse the majority of 2D metals are unstable in the air due to the surface dangling bonds and relatively high oxidability.

Herein, we develop a plasma-enhanced chemical vapor deposition method to construct the 2D room-temperature magnetic MnGa₄-H crystal with a thickness of 2.2 nm. Hydrogen insertion inside the MnGa₄ lattice can modulate the atomic distance

1. Introduction

2D magnetic materials have aroused a surge of research interest in recent years since they open the door to explore new spintronic devices.^[1–6] To further achieve practical applications, a stable magnetic phase/state at room temperature of 2D magnets is demanded. However, only very few 2D intrinsic room-temperature magnets have been discovered.^[7–9] Magnetic modulation can enrich the magnetic material family, encompassing but not limited to the electric field,^[10] element doping,^[11–13] strain,^[14,15] pressure,^[16,17] etc. These methods in general suffer from a destroyed structure or require the

N. Wei, L. He, R. Li, H. Lan, M. Zeng, L. Fu
College of Chemistry and Molecular Sciences
Wuhan University
Wuhan 430072, P. R. China
E-mail: zengmq_lan@whu.edu.cn; leifu@whu.edu.cn


C. Wu, X. Wang
Shenzhen Key Laboratory of Nanobiomechanics
Shenzhen Institute of Advanced Technology
Chinese Academy of Sciences
Shenzhen 518055, P. R. China
E-mail: xiao.wang@siat.ac.cn

C. Wu
Guangdong Provincial Key Laboratory of Electronic Functional
Materials and Devices
Huizhou University
Huizhou 516001, P. R. China

D. Lu, Y. Long
Beijing National Laboratory for Condensed Matter Physics
Institute of Physics
Chinese Academy of Sciences
Beijing 100190, P. R. China
E-mail: ywlong@iphy.ac.cn

H. Shi, L. Fu
The Institute for Advanced Studies
Wuhan University
Wuhan 430072, P. R. China

Y. Wen, J. He
Key Laboratory of Artificial Micro- and Nano-structures
of Ministry of Education, and School of Physics and Technology
Wuhan University
Wuhan 430072, P. R. China

 The ORCID identification number(s) for the author(s) of this article can be found under <https://doi.org/10.1002/adma.202210828>.

DOI: 10.1002/adma.202210828

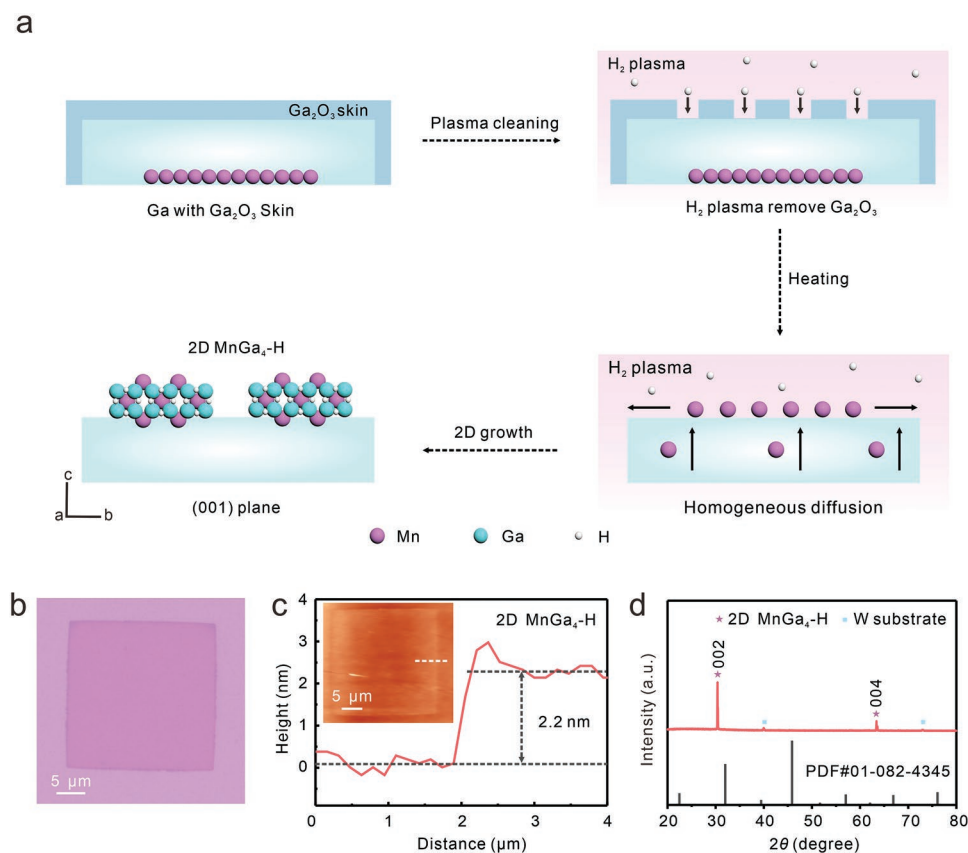


Figure 1. Synthesis and characterizations of 2D MnGa₄-H single crystals. a) Schematic illustration of the growth process of 2D MnGa₄-H. b) OM image of 2D MnGa₄-H single crystal on SiO₂/Si substrate. c) AFM image and corresponding height profile of the 2D MnGa₄-H single crystal on SiO₂/Si substrate. d) XRD θ -2 θ pattern of 2D MnGa₄-H single crystals on W substrate. ■ indicates the XRD peaks of W substrate. ★ indicates the XRD peaks of 2D MnGa₄-H.

and charge state without destroying the structural configuration, thereby ferrimagnetism can be achieved. The as-obtained 2D MnGa₄-H crystal is high-quality and air-stable, exhibiting robust and stable room-temperature magnetism with a high Curie temperature (T_C) above 620 K. Our work provides an effective method for the construction and modulation of 2D room-temperature magnetic alloys and opens up the possibility for the development of spintronic devices based on 2D magnetic and metallic materials, such as spin-valve and magnetic tunnel junction.

2. Results and Discussion

2.1. Construction of 2D MnGa₄-H Single Crystals

2D MnGa₄-H crystals were constructed by the plasma-enhanced chemical vapor deposition (PECVD) approach, in which the H₂ plasma plays an important role. **Figure 1a** schematically illustrates the growth route of 2D MnGa₄-H on the gallium (Ga) surface with H₂ plasma. Most metals have a certain solubility in Ga, thus Ga can be used as a metallic solvent to synthesize Ga-based alloys.^[19–21] In the oxygen-containing environment, a protective Ga₂O₃ layer will automatically form on the Ga surface,^[22,23] and cannot be reduced by conventional reducing gases such as hydrogen unless under extreme conditions.^[24]

Due to the strong interaction between Ga₂O₃ and Ga, the surface lateral diffusion rate of solute atoms is limited,^[25] which hampers the layer-by-layer 2D growth mode of Ga-based alloy. It is urgent to develop a facile method to remove the Ga₂O₃ layer. From Gibbs free energy, monatomic hydrogen can reduce many metal oxides more easily than molecular hydrogen,^[26,27] thus we exploit H₂ plasma with strong etching ability and reducibility to remove the Ga₂O₃ layer on the Ga surface at a relatively mild condition. After removing the Ga₂O₃ layer, the Mn atoms segregated to the surface can obtain a relatively faster lateral diffusion rate, thereby 2D MnGa₄-H can be successfully constructed. Instead, bulk samples will be obtained without H₂ plasma (Figure S1, Supporting Information). Optical microscopy (OM) and scanning electron microscope (SEM) images of the Ga surface after H₂ plasma-assisted or H₂ plasma-free growth routes are shown in Figures S2–S4 (Supporting Information), demonstrating the apparent Ga₂O₃ removal by H₂ plasma. OM image shows that the obtained 2D MnGa₄-H crystal presents a tetragonal morphology (Figure 1b) with a lateral size of ≈ 20 μ m. Atomic force microscopy (AFM) substantiates the 2D feature of the MnGa₄-H single crystal. Such a typical single crystal shows a thickness of ≈ 2.2 nm (Figure 1c), which is ≈ 3 –4 unit cell thickness. The θ -2 θ X-ray diffraction (XRD) was performed to identify the crystal structure of thus-produced samples. The XRD pattern of the bulk MnGa₄ grown without H₂ plasma was carried out (Figure S5, Supporting Information), which is

corresponding to the reported cubic MnGa_4 ($Im\bar{3}m$, No. 229). In comparison, the XRD pattern of 2D $\text{MnGa}_4\text{-H}$ (Figure 1d) only shows ($X00$) peaks and the measured ($X00$) peaks shifted to lower angles. This indicates that the as-obtained 2D $\text{MnGa}_4\text{-H}$ single crystals undergo the lattice expansion. Considering the high activity, density, and radical ionization properties of H_2 plasma,^[28] the employment of the H_2 plasma can enable a decrease in the activation energy barrier for H_2 dissociation. The hydrogen atom is the smallest atom and 2D MnGa_4 has a relatively large interstitial void, which ensures the dissociated hydrogen atoms insert into and expand the 2D MnGa_4 lattice. In the XRD test, the substrate was W foil, the peaks at 40° and 78° can be attributed to the W substrate. The XRD pattern of the pure W substrate is shown in Figure S6 (Supporting Information). We collected XRD patterns of 2D $\text{MnGa}_4\text{-H}$ at different plasma treatment times to provide further evidence of lattice expansion induced by hydrogen insertion. It can be seen that with the increase in processing time, the ($X00$) peak positions gradually move to the lower angle, which means a larger lattice expansion (Figure S7, Supporting Information). In order to verify the stability of the obtained $\text{MnGa}_4\text{-H}$, we carried out annealing experiments at high temperatures. After annealing at 473.15 K in Ar for 1 h, the XRD spectrum of $\text{MnGa}_4\text{-H}$ remains unchanged, indicating that the obtained $\text{MnGa}_4\text{-H}$ has good thermal stability. After annealing at 623.15 K in Ar for 1 h, the ($X00$) peak positions move to the higher angle, manifesting that hydrogen atoms escape from the interstitial void of $\text{MnGa}_4\text{-H}$ (Figure S8, Supporting Information). We noticed that the XRD peak of $\text{MnGa}_4\text{-H}$ deteriorated obviously when the annealing temperature reached 673.15 K. According to the reported phase diagram, this can be attributed to the decomposition of MnGa_4 at ≈ 670 K.^[29] Secondary-ion mass spectrometry (SIMS) measurements were carried out to further explore the hydrogen insertion and release (Figure S9, Supporting Information). We also conducted H_2 -plasma treatment on bulk MnGa_4 , but no shift of peak position was observed (Figure S10, Supporting Information). This can be attributed to the fact that the passivation layer on the surface of the bulk MnGa_4 prevents hydrogen insertion.^[30] X-ray photoelectron spectroscopy was also used to elucidate the composition and surface chemical states of the as-prepared samples (Figures S11,S12, Supporting Information). Ga 2p core line of 2D $\text{MnGa}_4\text{-H}$ shifted to a higher binding energy compared to that of bulk MnGa_4 , which is a typical feature of hydrogen insertion in metals.^[31,32] For 2D metals, rapid degradation under environmental exposure is a crucial issue. It is worth noting that even after 2D $\text{MnGa}_4\text{-H}$ was exposed to air for 7 days, no obvious oxidation was observed on its surface (Figure S13, Supporting Information). This may be due to the reducibility of the inserted hydrogen atoms so that they can be employed as an antioxidant. In addition, hydrogen fills the interstitial void of MnGa_4 , which could potentially hinder oxygen penetration.^[33] The evolution of XRD patterns with time progression also showed good air stability within 7 days (Figure S14, Supporting Information). We made a comprehensive comparative table to demonstrate the superior air stability of our prepared 2D $\text{MnGa}_4\text{-H}$ in 2D non-noble metal systems (Table S1, Supporting Information). The great air-stable of our as-prepared magnetic 2D $\text{MnGa}_4\text{-H}$ is essential for exploring the practical application in future spintronic devices.

2.2. Structural Characterization of 2D $\text{MnGa}_4\text{-H}$ Single Crystals

The overall structure of MnGa_4 can be viewed as a defective CsCl structure where three-fourths of the Cs-site atoms are eliminated to form corner-linked cubes.^[34] To get a deeper insight into 2D $\text{MnGa}_4\text{-H}$ crystal, the composition and crystal structure were further confirmed using energy dispersive X-ray spectroscopy (EDS) and high-angle annular dark-field aberration-corrected scanning transmission electron microscopy (HAADF-STEM). The 2D $\text{MnGa}_4\text{-H}$ on the W foil was transferred onto carbon-supported Cu grids via the polyvinyl alcohol (PVA) assisted transfer method. The "Experimental Section" and Figure S15 (Supporting Information) provide the details about the transfer process. The low-magnification STEM image of a $\text{MnGa}_4\text{-H}$ single crystal and the corresponding EDS elemental mapping images (Figure 2a) demonstrate the uniform spatial distribution of Ga and Mn elements throughout the whole crystal with the Mn/Ga ratio of ≈ 0.25 (Figure S16, Supporting Information). The selective area electron diffraction pattern is shown in Figure S17 (Supporting Information), suggesting that the $\text{MnGa}_4\text{-H}$ crystal is a single crystal with a tetragonal structure. Figure 2b,c shows a typical atomic-resolution HAADF-STEM image of the top view of a 2D $\text{MnGa}_4\text{-H}$ single crystal. Figure 2h,i display the cross-section view of the 2D $\text{MnGa}_4\text{-H}$ single crystal, where the Mn and Ga atoms correspond to dark and bright spots due to their difference in atomic numbers (Z). The well-ordered atomic arrangement without observable local discontinuities or defects in the STEM image verifies the high crystal quality of the 2D $\text{MnGa}_4\text{-H}$ single crystal. In addition, the corresponding fast Fourier transform (FFT) patterns further confirm the high crystallinity, owing to that both of them only have one set of tetragonal diffraction spots (Figure 2e,k). Figure 2d,j manifests simulated STEM images of MnGa_4 , demonstrating that $\text{MnGa}_4\text{-H}$ has the same crystal configuration as MnGa_4 . The hydrogen insertion would not lead to the collapse of the crystal structure of 2D MnGa_4 . To further examine the crystal structure of 2D $\text{MnGa}_4\text{-H}$, the HAADF images were analyzed in detail by extracting the intensity line profiles. In the top view of 2D $\text{MnGa}_4\text{-H}$ crystal, the lattice spacing of 4.15 and 2.93 Å can be observed, corresponding to the (110) and (020) planes, which is larger than the simulated MnGa_4 (Figure 2f,g). In the cross-section view, the lattice spacing of 4.15 and 2.93 Å correspond to the (1-10) and (002) planes, which are also larger than those of the simulated MnGa_4 (Figure 2l,m). These results suggest that hydrogen can incorporate into interstitial sites of the 2D MnGa_4 lattice to induce lattice expansion without destroying the structural configuration, thereby making the lattice constant enlarged in the entire structure, agreeing with the above XRD results.

2.3. Magnetic Properties of 2D $\text{MnGa}_4\text{-H}$ Single Crystals

To study the magnetic properties, both the magnetization versus magnetic field ($M-H$) curves and magnetization versus temperature ($M-T$) curves for bulk MnGa_4 and 2D $\text{MnGa}_4\text{-H}$ were measured with the Vibrating Sample Magnetometer (VSM, Quantum Design) system. First, the $M-H$ curve of the substrate (W foil) was investigated. The linear $M-H$ curves with

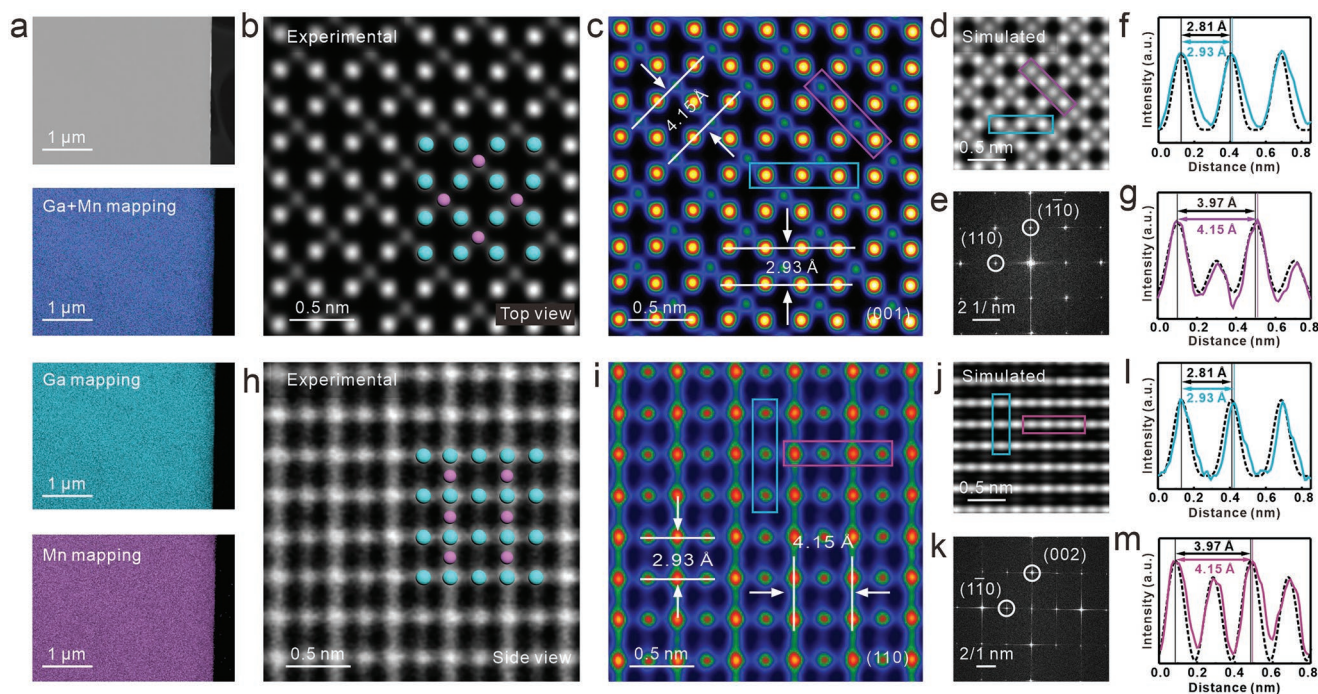


Figure 2. Composition and structural characterization of 2D $\text{MnGa}_4\text{-H}$ single crystals. a) HAADF image and corresponding EDS mapping of the $\text{MnGa}_4\text{-H}$ crystal. b, c) An atomic resolution HAADF-STEM image and the corresponding false-color image of the $\text{MnGa}_4\text{-H}$ crystal acquired along the c axis. d) The atomic structure simulation of MnGa_4 crystal along the c -axis. e) the corresponding FFT pattern. f, g) Intensity line profiles for the purple and blue rectangles marked in (c) and (d). The colored solid lines and black dotted lines represent the corresponding intensity line profiles of the $\text{MnGa}_4\text{-H}$ STEM image and simulated MnGa_4 STEM image, respectively. h, i) An atomic resolution HAADF-STEM image and the corresponding false-color image of the cross-section of the $\text{MnGa}_4\text{-H}$ crystal. j) The atomic structure simulation of the cross-section of the MnGa_4 crystal. k) the corresponding FFT pattern. l, m) Intensity line profiles for the purple (l) and blue (m) rectangles marked in (i) and (j). The colored solid lines and black dotted lines represent the corresponding intensity line profiles of the cross-section $\text{MnGa}_4\text{-H}$ STEM image and the simulated cross-section MnGa_4 STEM image, respectively.

zero hysteretic loops taken at different temperatures indicate a paramagnetic background of W substrate (Figure S18, Supporting Information). The M - T curve for bulk MnGa_4 is provided in Figure S19 (Supporting Information). With decreasing temperature from 600 to 300 K, the magnetization gradually increases, and then a kink shows up at $T_N \approx 340$ K, indicating the occurrence of an antiferromagnetic transition as reported in the literature.^[35] Moreover, the linear M - H behavior measured at 300 K is also in agreement with the antiferromagnetism. For the 2D $\text{MnGa}_4\text{-H}$ with an average thickness of ≈ 5 nm on W substrates, both low-temperature (2–350 K) and high-temperature (350–800 K) M - T curves were measured to analyze the magnetism. Unless otherwise specified, the 2D $\text{MnGa}_4\text{-H}$ exposed by H_2 plasma for 90 min are all used for the following measurements. Since different samples were adopted for such measurements, the M - T data were normalized based on the data obtained at 350 K. As shown in Figure 3a, the normalized M - T curve in 2–800 K nearly remains constant except for a remarkable decrease on heating to ≈ 620 K, where the hydrogen starts to release from the 2D $\text{MnGa}_4\text{-H}$. The phase transition of dehydrogenated $\text{MnGa}_4\text{-H}$ is also observed at 670 K, which is consistent with MnGa_4 . Such a constant M - T feature is reminiscent of a saturated ferromagnetic (FM) behavior below its T_C . To further reveal the possible ferromagnetism of the 2D $\text{MnGa}_4\text{-H}$, M - H curves were measured at different temperatures. As shown in Figure 3b, canonical FM hysteresis loops

are found to occur at all of our selected temperatures (10, 50, 100, 200, 300, and 390 K). The magnetic property of 2D $\text{MnGa}_4\text{-H}$ after dehydrogenation was further conducted, which shows a non-magnetic response, suggesting the magnetism of 2D $\text{MnGa}_4\text{-H}$ is induced by hydrogen insertion (Figure S20, Supporting Information). These features confirm the long-range FM ordering of the 2D $\text{MnGa}_4\text{-H}$, and the intrinsic T_C should be higher than the hydrogen-released temperature (620 K) of the sample. To probe the tunable magnetism, 2D $\text{MnGa}_4\text{-H}$ samples with different H_2 plasma exposure times were produced. A series of M - H data were collected for the 2D $\text{MnGa}_4\text{-H}$ under different H_2 plasma exposure times (Figure 3c). MnGa_4 without H_2 plasma treatment has zero coercivity, which is a typical characteristic of antiferromagnetism. At a longer exposure time such as 30 min, MnGa_4 turns to exhibit a very weak ferromagnet with coercivity (H_C) of 0.5 Oe. A narrow scale is shown in Figure S21 (Supporting Information) for better presentation. As we continue to increase the H_2 plasma exposure time, maximum coercive fields can be observed in 120 min with H_C up to 100 Oe. Exposure-time dependence of the H_C at 300 K is provided in Figure 3d. With increased H_2 plasma exposure time, 2D $\text{MnGa}_4\text{-H}$ can be tuned from antiferromagnetic (AFM) to ferromagnetic (FM) states. The in-plane and out-of-plane magnetization curves at 300 K show an out-of-plane easy magnetization axis (Figure S22, Supporting Information). Although 2D $\text{MnGa}_4\text{-H}$ exhibits the same macroscopic prop-

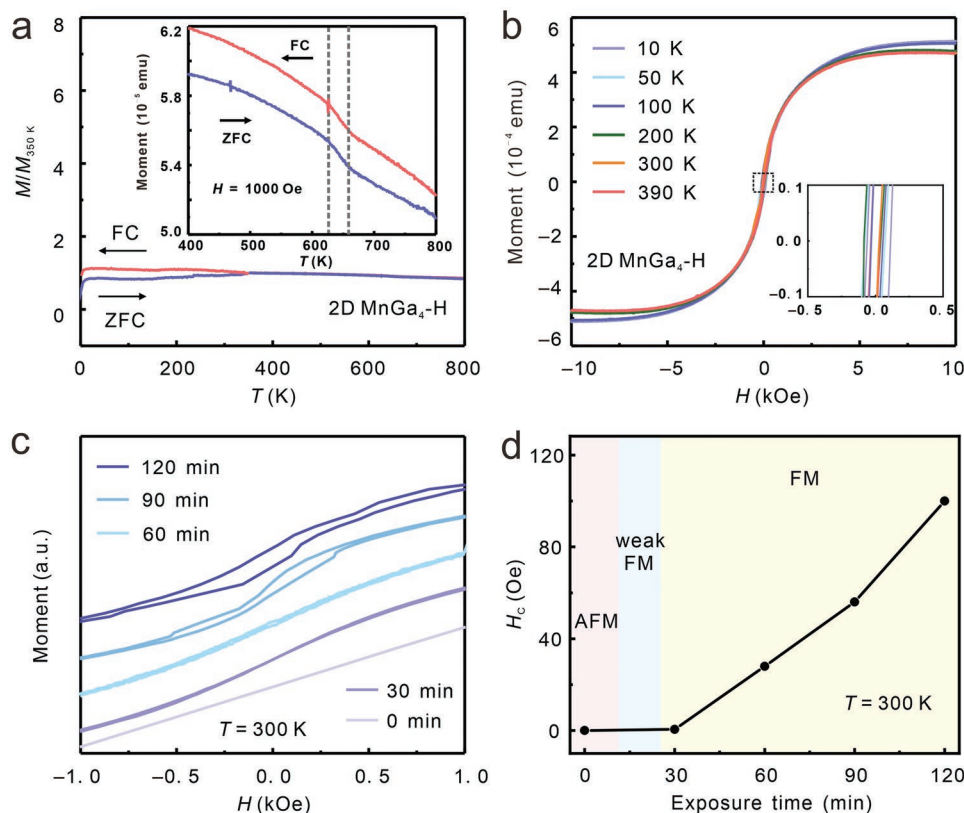


Figure 3. Magnetic properties of 2D MnGa₄-H. a) The temperature dependence of FC and ZFC M - T curves for 2D MnGa₄-H measured in the $H = 1$ kOe from 2 to 800 K. The inset shows the M - T curves on a narrow scale for better presentation. b) M - H curves of 2D MnGa₄-H at different temperatures with magnetic fields ranging from -10 to 10 kOe after background subtraction. The inset shows the M - H curves on a narrow scale for better presentation. c) M - H curves of 2D MnGa₄-H at different H₂ plasma exposure times with magnetic fields ranging from -1 to 1 kOe after background subtraction. d) Exposure-time dependence of the coercivity (H_c) at 300 K. With the increase of H₂ plasma exposure time, the magnetic property of 2D MnGa₄-H can be tuned from AFM to FM states.

erties as ferromagnetic, its ground state magnetic structure is ferrimagnetic. As shown later, theoretical calculations demonstrate that the FM behavior of the 2D MnGa₄-H arises from the competition between antiferromagnetic exchange interactions and ferromagnetic spin configuration.

2.4. Magneto-Transport Measurement of 2D MnGa₄-H Single Crystals

It is worth noting that the VSM test can only obtain the overall signal of all samples on the substrate. Considering the influence of sample thickness on magnetic properties, 2D MnGa₄-H single crystals with typical thicknesses of 5.5 and 19.0 nm were fabricated into devices to investigate the anomalous Hall effect through the magnetotransport measurement, respectively. AFM analysis of the fabricated device of 2D MnGa₄-H is provided in Figure S23 (Supporting Information). The Hall resistance (R_{xy}) was investigated within the ± 2.0 T external magnetic field range, applied perpendicular to the sample plane. For 5.5 nm MnGa₄-H, the R_{xy} shows clear hysteresis loops at all temperatures (Figure 4a). Such hysteresis reflects spontaneous magnetization and thus the long-range magnetic order, which agrees well with the VSM measurement.

For 19.0 nm MnGa₄-H, no obvious hysteresis loop was observed (very low coercivity and remanence), manifesting the extremely weak magnetism and the waning magnetism of MnGa₄ with the increase of thickness (Figure 4b). As shown in Figure 4c, the coercive field shrinks obviously as the temperature rises for 5.5 nm MnGa₄-H, which is characteristic of robust magnetism. In contrast, the coercive field of 19 nm MnGa₄-H is negligible and does not change significantly over the entire measured temperature. These results indicate that hydrogen insertion becomes difficult as the thickness increases, resulting in a weaker magnetic transition. Further calculated results show the diffusion barrier of the hydrogen atom at 2D MnGa₄ is lower than at bulk MnGa₄ (Figure S24, Supporting Information), indicating that hydrogen atoms are easier to migrate and insert in the 2D system, which is consistent with the experimental results. A schematic of a four-probe device for longitudinal resistance (R_{xx}) measurement is provided in Figure S25 (Supporting Information). The temperature-dependent R_{xx} of 2D MnGa₄-H and the first derivative of R_{xx} as a function of temperature are shown in Figure 4d. R_{xx} decreases gradually as the temperature decreases, exhibiting metallic behavior with good conductivity. No kink is observed in both R_{xx} and the first temperature derivative curves, indicating there is no phase transition from 2 to 300 K.

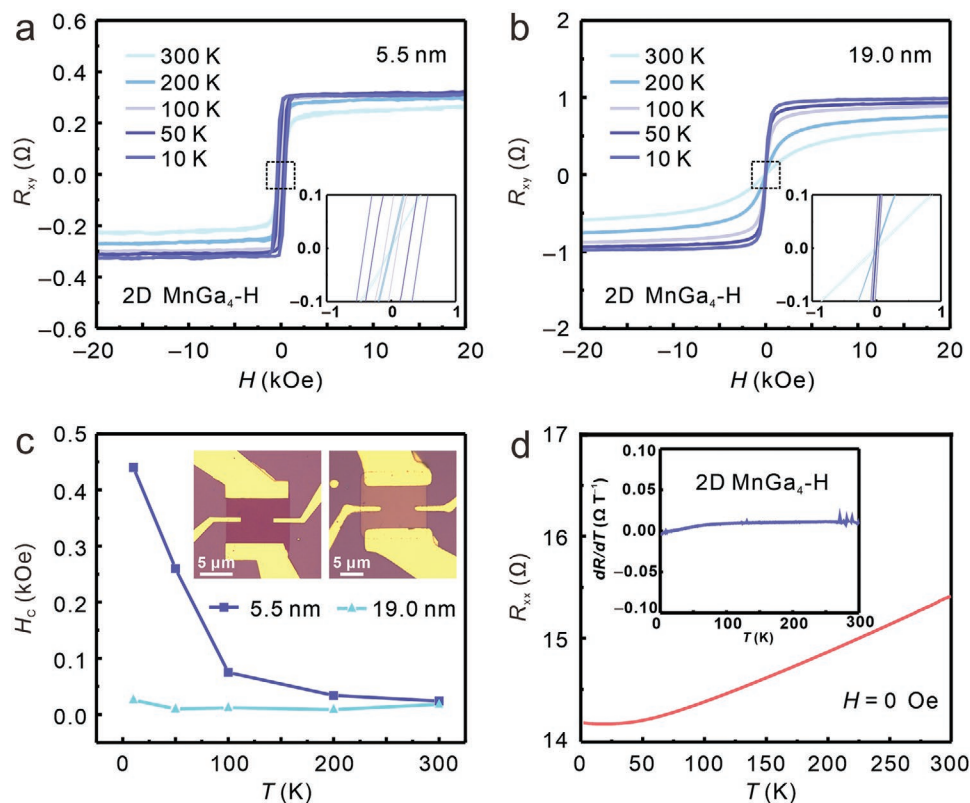


Figure 4. Magnetotransport measurement of 2D MnGa₄-H. a,b) Out-of-plane Hall resistance hysteresis loops at various temperatures obtained from 2D MnGa₄-H single crystals with thicknesses of 5.5 and 19.0 nm, respectively. The insets show the R_{xy} - H curves on a narrow scale for better presentation. c) The coercivity fields obtained from 2D MnGa₄-H single crystals with different thicknesses as a function of temperature. The insets show OM images of the corresponding Hall devices. d) The temperature dependence of the longitudinal R_{xx} of 2D MnGa₄-H measured in zero magnetic fields. The inset shows the first derivative of the longitudinal resistance as a function of temperature.

2.5. Insight into the Origin of Magnetic Order in 2D MnGa₄-H Crystals

To obtain an in-depth understanding of the origin of the room-temperature magnetic in the 2D MnGa₄-H system, we performed density functional theory (DFT) calculations (see computational details in the Experimental Section). We calculated the adsorption energy of hydrogen for 2D MnGa₄ (Figure S26, Supporting Information). By comparing the adsorption energies of hydrogen atoms at different sites, it can be concluded that hydrogen adsorbed at the center of the face is the most stable. Molecular dynamics simulation of hydrogen at different adsorption sites show that while hydrogen is adsorbed at the center of the face, the simulated framework of the structure is well maintained, which verifies the conclusion that the center of the face is the optimal adsorption site (Figure S27, Supporting Information). After that, the magnetism of the 2D MnGa₄-H was studied to reveal the mechanism of magnetic phase transition. The spin density differences of 2D MnGa₄ and 2D MnGa₄-H were calculated (Figure 5a). The results suggest that magnetic moments are almost derived from Mn atoms. The magnetic moments of Mn atoms in MnGa₄ with hydrogen insertion are displayed in Figure S28 (Supporting Information). The magnetic moment of Mn1 and Mn2 without hydrogen insertion is almost inverse (1.32 μ B vs -1.45 μ B) and displays

the apparent antiferromagnetic character. As the hydrogen is inserted into MnGa₄, the magnetic moment of Mn1 increases and even reaches 2.58 μ B while Mn2 decreases and finally reduces to nearly zero. Figure 5b plots the projected spin-polarized density of states (DOS) of 2D MnGa₄ and 2D MnGa₄-H. The Mn1 and Mn2 atoms possess opposite spin states and compensate each other for 2D MnGa₄, which is consistent with our aforementioned magnetic moment. While in the case of 2D MnGa₄-H, the spin-up states of Mn1 and Mn2 atoms both shift to lower energy, leading to the magnetic moment of Mn1 increasing and Mn2 decreasing. To understand the effect of hydrogen insertion on the magnetism of 2D MnGa₄-H, we calculated the exchange energy ($\Delta E = E_{AFM} - E_{FM}$) variation with the concentration of hydrogen insertion, where E_{AFM} and E_{FM} are the total energy of the antiferromagnetic and ferromagnetic states, respectively (Figure S29, Supporting Information). The exchange energy ΔE is -0.133 eV without hydrogen insertion, which indicates the magnetic moments of Mn atoms in MnGa₄ arrange oppositely. The total magnetic moment is ≈ 0.0 μ B. The magnetic moments of Mn atoms in MnGa₄ are reduced with hydrogen insertion, then the exchange energy ΔE increases and becomes positive. The system becomes ferrimagnetism (Figure 5c). In conclusion, when 2D MnGa₄ is inserted with hydrogen, the Mn-Mn antiferromagnetic coupling in the nearest neighbor will be weakened, and the ferromagnetic

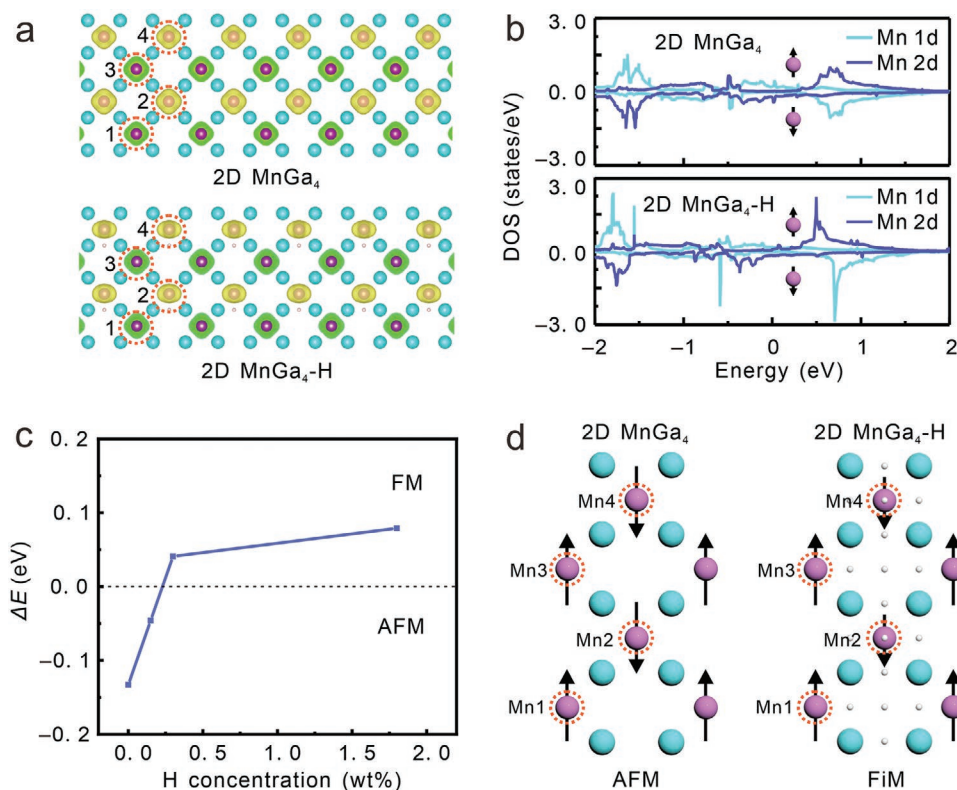


Figure 5. Theoretical calculations of the magnetism in 2D MnGa₄-H. a) The calculated spin densities of 2D MnGa₄ and 2D MnGa₄-H with an isosurface value of 0.005 e Bohr⁻³. The green and yellow isosurface contours represent spin-up and spin-down, respectively. b) Projected spin-polarized DOS of Mn1 and Mn2 atoms in 2D MnGa₄ and 2D MnGa₄-H. The Fermi level is set to zero. The spin-up and spin-down states are indicated by black arrows. c) AFM-FM energy difference (ΔE) evolution as a function of H concentration. d) Spin configurations of 2D MnGa₄ and 2D MnGa₄-H indicated by black arrows.

coupling of the second nearest neighbor Mn-Mn plays a dominant role, thus the whole system arises remanent magnetism (Figure 5d).

3. Conclusion

In summary, we develop a facile and controllable approach to construct and modulate 2D room-temperature magnetic MnGa₄-H crystal. Our as-obtained 2D MnGa₄-H crystal is high-quality, air-stable, and thermo-stable, demonstrating robust and stable room-temperature magnetism with a high Curie temperature above 620 K. We systematically study the 2D room-temperature magnetism through experimental and theoretical results, demonstrating that hydrogen insertion inside the MnGa₄ lattice can regulate the atomic distance and charge state, thus making 2D MnGa₄-H exhibit room-temperature magnetism. The magnetic properties of 2D MnGa₄-H can be well-regulated in a controlled manner. With the increase of H₂ treatment time, the coercivity of 2D MnGa₄-H gradually increased, and AFM to room-temperature FM phase modulation can be achieved without destroying the structural configuration. We can expect that this method could potentially provide a universal strategy to prepare more room-temperature magnetic metals and thus meet the requirements of potential applications in spintronic devices.

4. Experimental Section

Pretreatment: Before growth, the tungsten (W) foils (0.5 cm × 0.5 cm, 99.95%, Alfa Aesar) were ultra-sonicated and rinsed with acetone, ethanol, and deionized water for 30 min sequentially. After that, 1 × 10⁻² M KMnO₄ (99.5%, Aladdin) aqueous solution was prepared by dissolving the salt into deionized water. The solution was then spin-coated on the W foils with a speed of 8500 rpm for 1 min to ensure a uniform distribution of Mn sources. Finally, the Ga ball (99.9%, Alfa Aesar) was uniformly coated on the treated W foil at the temperature of 50 °C.

Growth of 2D MnGa₄-H Single Crystals: 1) Ga-W substrate was loaded into a one-inch tube furnace for the PECVD process. The CVD system was pumped with a base pressure of 1 Pa and then purged with high-purity argon gas (Ar, 99.999%) at a flow rate of 1000 sccm for 10 min. 2) The PECVD system was then purged with 100 sccm H₂ as carrier gases, and the pressure of the PECVD system was 170 Pa. The substrate was heated to 650 °C at a rate of 10 °C min⁻¹ and held for 10 min after the desired growth temperature was reached to fully reduce and diffuse the precursor under H₂ plasma (100 W). The overall pressure of the system remained unchanged after plasma was initiated, thus the corresponding H₂ plasma flux could be regarded as the same as the flux of H₂. 3) Plasma was turned off after synthesis, and the system was cooled to room temperature rapidly under the H₂ atmosphere.

Transferring 2D MnGa₄-H to Target Substrates: Ga-W substrates with MnGa₄ crystals were placed on the heating stage at a temperature of 40 °C until Ga was molten. W foils are adapted to transfer the obtained sample on the Ga surface due to the relatively strong adhesion between metals and the relatively weak adhesion between the oxide layer and metal. To remove residual Ga from the sample, a facile mechanical

cleaning method was employed. At first, ≈ 50 ml of deionized water was taken into a beaker, followed by heating them to 50 °C. Then, the W foil with printed 2D MnGa₄ crystals was immersed in the deionized water and cleaned by ultrasonic treatment to remove residual Ga. Then the PVA film was covered on the W foil and heated to 100 °C for an hour. After that, the PVA film was transferred from the W substrate to the desired substrate (SiO₂, Si, TEM grids, etc.). The polymer mediator was then removed by dissolving in deionized water. Finally, the 2D MnGa₄-H could be obtained on the target substrate.

Device Fabrication and Transport Measurement: A thick poly (methyl methacrylate) (PMMA 950, A4) film was deposited by spin coating at 3000 rpm for 1 min and then was baked at 100 °C for 1 min. The devices with Hall bar geometry and four electrodes for measuring R_{xx} were patterned by a standard electron beam lithography technique on SiO₂/Si substrate. Bilayer metals with 10 nm Cr and 60 nm Au were deposited by a thermal evaporator (JSD300 Vacuum, 1.0×10^{-7} Torr) and used as contact electrodes.

Characterizations and Measurements: The XRD characterization was conducted using a Rigaku Miniflex600 with Cu-K α radiation over the range of $2\theta = 20\text{--}80^\circ$. Optical images were taken with an optical microscope (Olympus DX51). SEM images were obtained from a ZEISS Merlin Compact SEM with EDS spectra collected by X-MaxN Oxford EDS. The acceleration voltage of the electron beam was 8 kV. The thickness was measured on an NT-MDT Ntegra Spectra atomic force microscope. TEM images and HADDF-STEM images were taken by FEI Tecnai G2F30 operated at an accelerating voltage of 300 kV. The sample lamellas for the cross-sectional TEM characterization were prepared via FIB treatment by ThermoFisher Scios 2. TEM energy-dispersive EDS elemental mapping was also performed by FEI Tecnai G2F30. ToF-SIMS measurements were carried out with a Focused Ion Beam Scanning Electron Microscope with the ToF-SIMS instrument (Tescan AMBER) equipped with a Ga liquid-metal ion source for analysis and a Ga³⁺ ion beam for sputtering. The detected region was $\approx 20 \times 20 \mu\text{m}^2$. Depth profile and cross-section chemical mapping were collected in spectrometry mode with a current of 298 pA to sputter through the 2D materials. The magnetic susceptibility and magnetization measurements were carried out using a superconducting quantum interference device magnetometer (Quantum Design, MPMS-VSM). Two modes (zero field cooling and field cooling) were adopted to measure the susceptibility at a magnetic field of 0.1 T. Magnetization was measured between -1 and $+1$ T at selected temperatures. The longitudinal resistance (R_{xx}) was collected by a pulse relaxation method on a physical property measurement system calorimeter (Quantum Design, PPMS-9T) varying from 300 to 2 K under zero magnetic fields. The Hall electrical resistance (R_{xy}) was measured by a physical property measurement system calorimeter (Quantum Design, PPMS-9T) at some selected temperatures and with varying external magnetic fields (H) from -2 to $+2$ T. A constant current of 100 μA was carried out in those experiments.

Theoretical Calculations: First-principle calculations were performed using the framework of DFT as implemented in the Vienna ab initio simulation package.^[36,37] The pseudopotentials were treated by the projector augmented-wave method with a cutoff energy of 500 eV for plane-wave expansion.^[38] The generalized gradient approximation described electron exchange-correlation potential.^[39] The Hubbard U for 3d electrons of Mn was chosen as 0.5 eV referred to in the previous works.^[40] During structural relaxation, the atomic positions were relaxed until the Hellman-Feynman force on each atom was less than 0.01 eV \AA^{-1} . The climbing-image nudged elastic band method was used to estimate the kinetic pathways.^[41] The ab initio molecular dynamics simulation was performed at the canonical ensemble for 1 ps with the time step set as 1 fs.

Supporting Information

Supporting Information is available from the Wiley Online Library or from the author.

Acknowledgements

N.W., L.C.H., and C.W.W. contributed equally to this work. The research was supported by the National Natural Science Foundation of China (grant nos. 22025303, 21905210, and 22003074), the National Youth Talent Support Program, the Youth Innovation Promotion Association CAS, International Cooperation Project of Guangdong Province (No. 2019A050510049) and Guangdong Basic and Applied Basic Research Foundation (2022A1515012463).

Conflict of Interest

The authors declare no conflict of interest.

Data Availability Statement

The data that support the findings of this study are available from the corresponding author upon reasonable request.

Keywords

2D alloys, hydrogen insertion, MnGa₄-H, phase modulation, room-temperature magnetism

Received: November 21, 2022

Revised: March 1, 2023

Published online: March 31, 2023

- [1] B. Huang, G. Clark, E. Navarro-Moratalla, D. R. Klein, R. Cheng, K. L. Seyler, D. Zhong, E. Schmidgall, M. A. McGuire, D. H. Cobden, W. Yao, D. Xiao, P. Jarillo-Herrero, X. Xu, *Nature* **2017**, 546, 270.
- [2] K. S. Burch, D. Mandrus, J.-G. Park, *Nature* **2018**, 563, 47.
- [3] Y. Deng, Y. Yu, Y. Song, J. Zhang, N. Z. Wang, Z. Sun, Y. Yi, Y. Z. Wu, S. Wu, J. Zhu, J. Wang, X. H. Chen, Y. Zhang, *Nature* **2018**, 563, 94.
- [4] Z. Fei, B. Huang, P. Malinowski, W. Wang, T. Song, J. Sanchez, W. Yao, D. Xiao, X. Zhu, A. F. May, W. Wu, D. H. Cobden, J. H. Chu, X. Xu, *Nat. Mater.* **2018**, 17, 778.
- [5] C. Tan, J. Lee, S. G. Jung, T. Park, S. Albarakati, J. Partridge, M. R. Field, D. G. McCulloch, L. Wang, C. Lee, *Nat. Commun.* **2018**, 9, 1554.
- [6] X. Xu, S. Yang, H. Wang, R. Guzman, Y. Gao, Y. Zhu, Y. Peng, Z. Zang, M. Xi, S. Tian, Y. Li, H. Lei, Z. Luo, J. Yang, Y. Wang, T. Xia, W. Zhou, Y. Huang, Y. Ye, *Nat. Commun.* **2022**, 13, 7646.
- [7] X. Zhang, Q. Lu, W. Liu, W. Niu, J. Sun, J. Cook, M. Vaninger, P. F. Miceli, D. J. Singh, S. W. Lian, T. R. Chang, X. He, J. Du, L. He, R. Zhang, G. Bian, Y. Xu, *Nat. Commun.* **2021**, 12, 2492.
- [8] H. Wu, W. Zhang, L. Yang, J. Wang, J. Li, L. Li, Y. Gao, L. Zhang, J. Du, H. Shu, H. Chang, *Nat. Commun.* **2021**, 12, 5688.
- [9] R. Cheng, L. Yin, Y. Wen, B. Zhai, Y. Guo, Z. Zhang, W. Liao, W. Xiong, H. Wang, S. Yuan, J. Jiang, C. Liu, J. He, *Nat. Commun.* **2022**, 13, 5241.
- [10] B. Huang, G. Clark, D. R. Klein, D. MacNeill, E. Navarro-Moratalla, K. L. Seyler, N. Wilson, M. A. McGuire, D. H. Cobden, D. Xiao, W. Yao, P. Jarillo-Herrero, X. Xu, *Nat. Nanotechnol.* **2018**, 13, 544.
- [11] S. Jiang, L. Li, Z. Wang, K. F. Mak, J. Shan, *Nat. Nanotechnol.* **2018**, 13, 549.
- [12] W. Hu, C. Wang, H. Tan, H. Duan, G. Li, N. Li, Q. Ji, Y. Lu, Y. Wang, Z. Sun, F. Hu, W. Yan, *Nat. Commun.* **2021**, 12, 1854.

- [13] R. Chen, F. Luo, Y. Liu, Y. Song, Y. Dong, S. Wu, J. Cao, F. Yang, A. N'Diaye, P. Shafer, Y. Liu, S. Lou, J. Huang, X. Chen, Z. Fang, Q. Wang, D. Jin, R. Cheng, H. Yuan, R. J. Birgeneau, J. Yao, *Nat. Commun.* **2021**, *12*, 3952.
- [14] J. Cenker, S. Sivakumar, K. Xie, A. Miller, P. Thijssen, Z. Liu, A. Dismukes, J. Fonseca, E. Anderson, X. Zhu, X. Roy, D. Xiao, J. H. Chu, T. Cao, X. Xu, *Nat. Nanotechnol.* **2022**, *17*, 256.
- [15] Y. Wang, C. Wang, S. J. Liang, Z. Ma, K. Xu, X. Liu, L. Zhang, A. S. Admasu, S. W. Cheong, L. Wang, M. Chen, Z. Liu, B. Cheng, W. Ji, F. Miao, *Adv. Mater.* **2020**, *32*, 2004533.
- [16] T. Li, S. Jiang, N. Sivadas, Z. Wang, Y. Xu, D. Weber, J. E. Goldberger, K. Watanabe, T. Taniguchi, C. J. Fennie, K. Fai Mak, J. Shan, *Nat. Mater.* **2019**, *18*, 1303.
- [17] T. Song, Z. Fei, M. Yankowitz, Z. Lin, Q. Jiang, K. Hwangbo, Q. Zhang, B. Sun, T. Taniguchi, K. Watanabe, M. A. McGuire, D. Graf, T. Cao, J. H. Chu, D. H. Cobden, C. R. Dean, D. Xiao, X. Xu, *Nat. Mater.* **2019**, *18*, 1298.
- [18] A. Remhof, A. Borgschulte, *ChemPhysChem* **2008**, *9*, 2440.
- [19] T. Ma, J. Gou, S. Hu, X. Liu, C. Wu, S. Ren, H. Zhao, A. Xiao, C. Jiang, X. Ren, M. Yan, *Nat. Commun.* **2017**, *8*, 13937.
- [20] P. W. Menezes, C. Walter, J. N. Hausmann, R. Beltran-Suito, C. Schlesiger, S. Praetz, V. Yu Verchenko, A. V. Shevelkov, M. Driess, *Angew. Chem. Int. Ed.* **2019**, *58*, 16569.
- [21] H. F. Liu, J. Xia, N. Zhang, H. Cheng, W. Bi, X. L. Zu, W. S. Chu, H. A. Wu, C. Z. Wu, Y. Xie, *Nat. Catal.* **2021**, *4*, 202.
- [22] A. Zavabeti, J. Z. Ou, B. J. Carey, N. Syed, R. Orrell-Trigg, E. L. H. Mayes, C. L. Xu, O. Kavehei, A. P. O'Mullane, R. B. Kaner, K. Kalantar-Zadeh, T. Daeneke, *Science* **2017**, *358*, 332.
- [23] S. S. Zhao, J. Q. Zhang, L. Fu, *Adv. Mater.* **2021**, *33*, 2005544.
- [24] D. P. Butt, Y. Park, T. N. Taylor, *J. Nucl. Mater.* **1999**, *264*, 71.
- [25] J. Tang, S. Lambie, N. Meftahi, A. J. Christofferson, J. Yang, M. B. Ghasemian, J. Han, F. M. Alliou, M. A. Rahim, M. Mayyas, T. Daeneke, C. F. McConville, K. G. Steenbergen, R. B. Kaner, S. P. Russo, N. Gaston, K. Kalantar-Zadeh, *Nat. Nanotechnol.* **2021**, *16*, 431.
- [26] A. Rukini, M. A. Rhamdhani, G. A. Brooks, A. Van den Bulck, *J. Sustainable Metall.* **2022**, *8*, 1.
- [27] M. Baklanov, D. Shamiryan, Z. Tökei, G. Beyer, T. Conard, S. Vanhaelemeersch, K. Maex, *J. Vac. Sci. Technol., B: Microelectron. Nanometer Struct.–Process., Meas., Phenom.* **2001**, *19*, 1201.
- [28] H. P. Zhou, X. Ye, W. Huang, M. Q. Wu, L. N. Mao, B. Yu, S. Xu, I. Levchenko, K. Bazaka, *ACS Appl. Mater. Interfaces* **2019**, *11*, 15122.
- [29] M. Tillard, C. Belin, *Intermetallics* **2012**, *29*, 147.
- [30] C. W. Ostefeld, M. Johansson, I. Chorkendorff, *Surf. Sci.* **2007**, *601*, 1862.
- [31] Z. Zhao, X. Huang, M. Li, G. Wang, C. Lee, E. Zhu, X. Duan, Y. Huang, *J. Am. Chem. Soc.* **2015**, *137*, 15672.
- [32] T. Riesterer, *Z Physik. B - Condensed Matter* **1987**, *66*, 441.
- [33] J. Huot, G. Liang, R. Schulz, *Appl. Phys. A* **2001**, *72*, 187.
- [34] U. Häussermann, P. Viklund, M. Boström, R. Norrestam, S. I. Simak, *Phys. Rev. B* **2001**, *63*, 125118.
- [35] V. Y. Verchenko, A. A. Tsirlin, D. Kasinathan, S. V. Zhurenko, A. A. Gippius, A. V. Shevelkov, *Phys. Rev. Mater.* **2018**, *2*, 044408.
- [36] G. Kresse, J. Hafner, *Phys. Rev. B* **1993**, *48*, 13115.
- [37] G. Kresse, J. Furthmüller, *Phys. Rev. B* **1996**, *54*, 11169.
- [38] P. E. Blöchl, *Phys. Rev. B* **1994**, *50*, 17953.
- [39] J. P. Perdew, K. Burke, M. Ernzerhof, *Phys. Rev. Lett.* **1996**, *77*, 3865.
- [40] S. L. Dudarev, G. A. Botton, S. Y. Savrasov, C. J. Humphreys, A. P. Sutton, *Phys. Rev. B* **1998**, *57*, 1505.
- [41] S. A. Trygubenko, D. J. Wales, *J. Chem. Phys.* **2004**, *120*, 2082.